crystals

MDPI

Article

Preparation and Study of Poly(Vinylidene Fluoride-Co-Hexafluoropropylene)-Based Composite Solid Electrolytes

Meihong Huang [1,*,†], Lingxiao Lan [2,†], Pengcheng Shen [2,†], Zhiyong Liang [1], Feng Wang [1], Yuling Zhong [1], Chaoqun Wu [3,*], Fanxiao Kong [4] and Qicheng Hu [2]

[1] School of Automotive Engineering, Guangdong Polytechnic of Industry and Commerce, Guangzhou 510510, China; liangzy08@163.com (Z.L.); wangfeng_yhd@163.com (F.W.); wha33896@163.com (Y.Z.)
[2] Guangxi Key Laboratory of Automobile Components and Vehicle Technology, Guangxi University of Science & Technology, Liuzhou 545006, China; llx2685062@163.com (L.L.); 18852066673@163.com (P.S.); huqicheng@gmail.com (Q.H.)
[3] Center for Industrial Analysis and Testing, Guangdong Academy of Sciences, Guangzhou 510650, China
[4] Key Laboratory of Metal 3D Printing Technology, Liuzhou Polytechnic University, Liuzhou 545616, China; kongfanxiao@lzpu.edu.cn
* Correspondence: huangmh0828@163.com (M.H.); qun95@126.com (C.W.)
† These authors contributed equally to this work.

Abstract: Solid-state electrolytes are widely anticipated to revitalize lithium-ion batteries with high energy density and safety. However, low ionic conductivity and high interfacial resistance at room temperature pose challenges for practical applications. This study combines the rigid oxide electrolyte LLZTO with the flexible polymer electrolyte poly(vinylidene fluoride-co-hexafluoropropylene) (PVDF-HFP) to achieve effective coupling of rigidity and flexibility. The semi-interpenetrating network structure endows the PEL composite solid electrolyte with excellent lithium-ion transport capabilities, resulting in an ionic conductivity of up to 5.1×10^{-4} S cm^{-1} and lithium-ion transference number of 0.41. The assembled $LiFePO_4$/PEL/Li solid-state battery demonstrates an initial discharge capacity of 132 mAh g^{-1} at a rate of 0.1 C. After 100 charge–discharge cycles, the capacity retention is 81%. This research provides a promising strategy for preparing composite solid electrolytes in solid-state lithium-ion batteries.

Keywords: lithium-ion batteries; composite solid electrolytes; LLZTO

Citation: Huang, M.; Lan, L.; Shen, P.; Liang, Z.; Wang, F.; Zhong, Y.; Wu, C.; Kong, F.; Hu, Q. Preparation and Study of Poly(Vinylidene Fluoride-Co-Hexafluoropropylene)-Based Composite Solid Electrolytes. *Crystals* **2024**, *14*, 982. https://doi.org/10.3390/cryst14110982

Academic Editor: Ram S. Katiyar

Received: 23 October 2024
Revised: 7 November 2024
Accepted: 12 November 2024
Published: 14 November 2024

1. Introduction

With rapid technological advancements and increasing global energy dependence, the excessive extraction of fossil fuels has led to a significant energy crisis and severe ecological pollution [1–3]. Consequently, a growing focus is on low-carbon, environmentally friendly, and renewable energy sources, such as wind, hydropower, and solar energy [4–6]. However, the challenge of storing these clean resources necessitates using large-scale energy storage systems to integrate and convert them into electricity, enhancing their conversion efficiency, which is vital in modern life [7,8]. Lithium-ion batteries are one of the most promising options among various energy storage devices, known for their high energy density and long cycle life [9,10]. As lithium battery technology evolves, these batteries have found widespread applications in smartphones, computers, and vehicles [11]. Solid electrolytes offer better mechanical properties than liquid electrolytes and can function effectively under certain complex deformations, significantly reducing the risks of short circuits and fires [12]. Given the growing demand for energy density and safety, research on solid electrolytes is expected to receive increased attention [13,14].

For decades, solid polymer electrolytes (SPEs) have been studied as promising solid electrolyte materials [15]. Since the discovery that lithium ions (Li^+) can be conducted in

complexes of poly(ethylene oxide) (PEO) with alkali metal salts, researchers have employed various methods, such as blending [16–18], cross-linking [19–21], and organic-inorganic composites [22–24], to enhance the ionic conductivity of SPEs at room temperature. The polymer matrix poly(vinylidene fluoride-co-hexafluoropropylene) (PVDF-HFP) features a high dielectric constant and forms both amorphous and crystalline phases at ambient temperatures [25]. The amorphous phase facilitates ion movement within the polymer matrix, while the crystalline phase contributes to mechanical stability [26]. Polyacrylonitrile (PAN) is known for its excellent thermal resistance, low flammability, and potent antioxidant properties, making it a common choice for high-voltage cathode materials due to its compatibility [27]. Among inorganic solid electrolytes, $Li_{1.3}Al_{0.3}Ti_{1.7}(PO_4)_3$ (LATP) exhibits notable ionic conductivity at room temperature (approximately 10^{-3} S cm^{-1}). However, its high oxidation state titanium (Ti^{4+}) can react with lithium metal anodes, reducing Ti^{4+} to Ti^{3+} [28]. $Li_7La_3Zr_2O_{12}$ (LLZO) has garnered attention for its ionic conductivity comparable to that of liquid electrolytes (10^{-3} S cm^{-1}) and its exceptional stability against lithium metal, positioning it as a promising inorganic filler in solid-state batteries [29]. Gu et al. [30] developed a PVDF-HFP/LLZTO composite solid electrolyte using a UV-curing process. The composite solid electrolyte (CSE) membranes in lithium metal batteries exhibited improved mechanical properties and excellent electrochemical performance. At room temperature, the CSE-15 wt% LLZTO demonstrated the highest ionic conductivity ($\sigma = 3.7 \times 10^{-3}$ S cm^{-1}), a high lithium-ion mobility ($t_{Li}{}^{+}$ =0.79), an electrochemical stability window exceeding 5 V, and good mechanical strength (8.2 MPa). Zhou et al. [31] employed a simple spray-drying method to enhance the mass ratio of inorganic particles while addressing the issue of filler aggregation. During the atomization process, PVDF and lithium bis(trifluoromethane sulfonyl)azanide (LiTFSI) covered the surface of each LLZTO particle, forming a flat solid electrolyte through layer-by-layer deposition. Atomic force microscopy characterization revealed that the resulting solid electrolyte achieved a uniform dispersion of Young's modulus and surface electric field.

Consequently, the prepared SPEs demonstrated a high tensile strength of 7.1 MPa, ionic conductivity of 1.86×10^{-4} S cm^{-1} at room temperature, and a wide electrochemical window of up to 5.0 V, reflecting improved mechanical strength and uniform lithium ion transport pathways. Thanks to these developed SPEs, lithium symmetric cells exhibited stable lithium deposition/stripping cycles exceeding 1000 h at a current density of 0.1 mA cm^{-2}. Correspondingly, $LiCoO_2$/SPEs/Li batteries demonstrated good rate performance and excellent cycling stability, maintaining 80% of their capacity after 100 cycles at room temperature.

In this study, we developed a PVDF-HFP-ethoxylated trimethylolpropane triacrylate (ETPTA)-LLZTO composite solid electrolyte (PEL) by combining a polymer with an inorganic ionic conductive material using a UV-curing process. The interactions among PVDF-HFP, ETPTA, and LLZTO enhanced the electrochemical performance of the composite. We investigated various ratios of LLZTO through physical and electrochemical characterization methods to determine the optimal filler-to-polymer ratio. The resulting composite solid electrolyte was then applied in LFP/PEL/Li solid-state batteries, allowing us to evaluate the electrochemical performance of the electrolyte under operational conditions. This work provides an effective strategy for utilizing composite solid electrolyte membranes in solid lithium batteries.

2. Materials and Methods

2.1. Materials

The materials used in this study include PVDF and PVDF-HFP (Mn = 600,000, Arkema, Colombes, France), lithium perchlorate ($LiClO_4$, 99.99%, Aladdin Chemical Co., Shanghai, China), N, N-dimethylformamide (DMF, ≥99.9%), N-methylpyrrolidone (NMP, ≥99.9%), Super-P (≥99.5%), and lithium iron phosphate ($LiFePO_4$, LFP, ≥99.5%), all sourced from Kede in Shanghai, China. The plasticizer trimethylolpropane ethoxylate triacrylate (ETPTA, Mn = 428) was obtained from Macklin, Shanghai, China.

2.2. Preparation of PEL Composite Solid Electrolytes

The PEL composite solid electrolyte membrane was prepared using a UV-curing method, as illustrated in Figure 1. First, 2 g of PVDF-HFP, which had been dried for 24 h at 60 °C, was placed in a drying oven. This was then mixed with an appropriate amount of lithium perchlorate ($LiClO_4$) and dissolved in DMF solvent, stirring until a transparent, homogeneous solution was obtained. The temperature was maintained at 60 °C while LLZTO was added and stirred thoroughly for 12 h. Next, the cross-linking agent ETPTA and the photoinitiator HMPP were added, and the mixture was stirred for 5 min. The uniform slurry was then poured into a polytetrafluoroethylene (PTFE) mold. Finally, the mixture was subjected to UV light at an intensity of 1200 mW cm^{-2} for 1 min to form a semi-wet membrane, which was then placed in a vacuum-drying oven for 6 h to obtain the PEL composite solid electrolyte. The resulting PEL membrane was cut into small discs with a diameter of 18 mm and stored in a glovebox (with H_2O < 0.01 PPM and O_2 < 0.01 PPM).

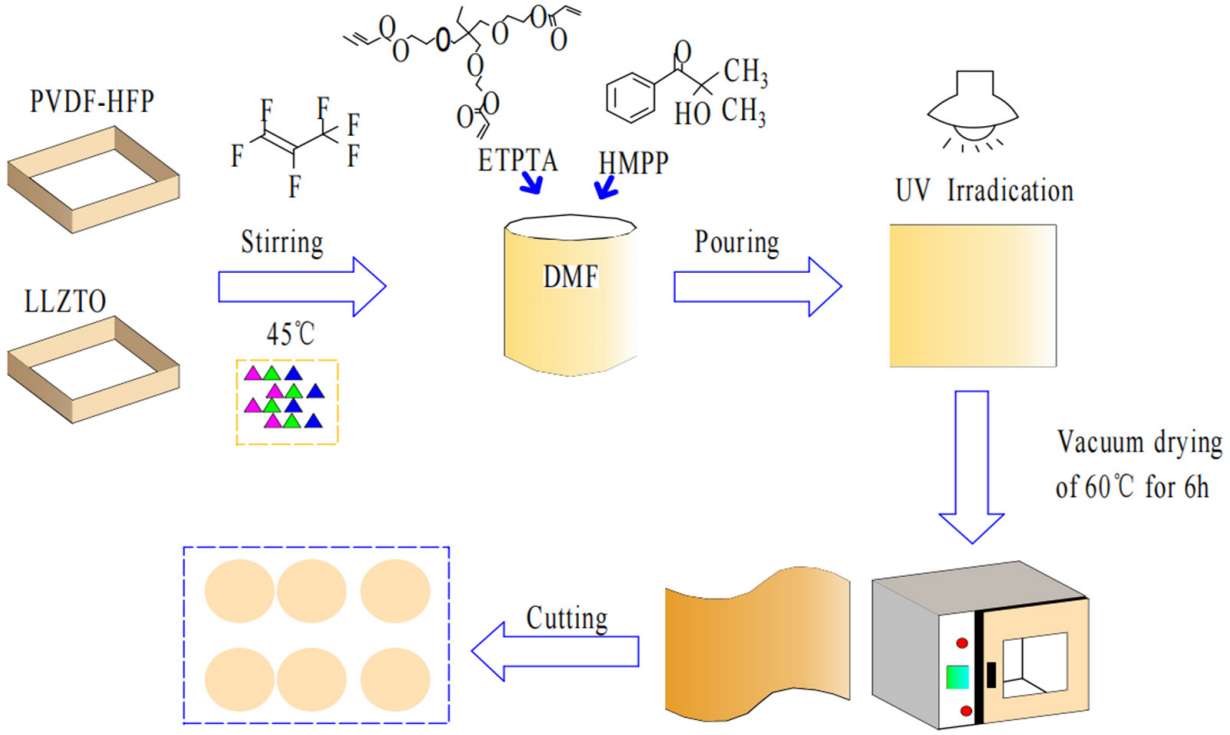

Figure 1. The preparation process of PEL.

2.3. Materials Characterization

The phase of the materials was characterized using an X-ray diffractometer (XRD, DX-2700, Dandong, China, Cu-Kα, 40 kV × 30 mA). The surface and cross-sectional characteristics of the composite solid electrolytes (CSEs) were examined using a scanning electron microscope (SEM, Phenom Spectra G2, Shanghai, China). The functional groups on the surface of the composite polymer electrolytes (CSEs) were identified using Fourier-transform infrared spectroscopy (FTIR, Spectrum 100, PerkinElmer, Waltham, MA, USA) in the 400 to 4000 cm^{-1} range. Additionally, the tensile strength of the CSEs was measured using a universal testing machine (WDW-5, Tenson, Jinan, China).

2.4. Electrochemical Properties

Electrochemical impedance spectroscopy (EIS) measurements were conducted at open circuit voltage (OCV) over a frequency range of 0.1 Hz to 1 MHz and at various temperatures, with an amplitude of 10 mV. The composite polymer electrolytes (CSEs) were

sandwiched between two smooth stainless steel (SS) electrodes. The different electrolytes' ionic conductivity (σ) was calculated from the EIS results using Equation (1):

$$\sigma = \frac{L}{RS} \tag{1}$$

where R is the bulk resistance obtained by EIS, and L and S are the thickness and effective area of CSEs, respectively.

The electrochemical window of various composite solid electrolytes (CSEs) was tested using linear sweep voltammetry (LSV) over a voltage range of 10 mV to 1 V. The SS/CSEs/Li assemblies were constructed in CR2025 coin cells for the LSV tests. Two polished lithium foils were used in symmetric cells to investigate the stability of different solid electrolytes concerning the lithium anode. A chronoamperometric method was employed to measure the lithium-ion transference number ($t_{Li}{}^{+}$) with the same symmetric cells assembled with other electrolytes. A polarization of 10 mV was applied for 4000 s. During this time, the alternating current (AC) impedance spectra were recorded before and after polarization under a 10 mV oscillating voltage across a frequency range of 0.1 Hz to 1 MHz. The lithium-ion transference number ($t_{Li}{}^{+}$) was calculated using Equation (2):

$$t_{Li^+} = \frac{I_s(\Delta V - R_0 I_0)}{I_0(\Delta V - R_s I_s)} \tag{2}$$

where I_0 and I_S represent the initial and steady-state currents, respectively, R_0 and R_S represent the charge transfer resistance of the electrolyte system before and after polarization, and ΔV is the oscillation voltage of 10 mV. LFP/CSEs/Li are assembled in CR2025 coin batteries for Cyclic Voltammetry (CV) testing. The scan rate is 0.2 mV s^{-1}.

The rate and cycling tests of the batteries were conducted using a battery testing system (Neware, Dongguan, China). Commercial lithium iron phosphate ($LiFePO_4$) was used as the positive active material, with lithium foil as the negative electrode. The LFP, PVDF, and conductive carbon mass ratio was set at 8:1:1. The mixture was dissolved in a solvent, and the resulting solution was coated onto aluminum foil, followed by vacuum drying for 36 h. The dried material was then cut into 14 mm discs for testing, performed over a voltage range of 2.8 to 4.0 V.

3. Results and Discussions

Figure 2 shows surface images of two solid electrolytes: PVDF-HFP/ETPTA (referred to as PE) and PEL. The PE membrane (Figure 2a,b) appears as a transparent solid electrolyte, while PEL exhibits a brown color. This noticeable color change indicates a de-fluorination reaction between LLZTO and PVDF-HFP. Figure 2c,d illustrate the flexibility and mechanical properties of the folded solid electrolytes. Visual inspection reveals that PE has slightly better flexibility than PEL; however, PEL demonstrates superior mechanical strength. LLZTO ceramic particles in the composite solid electrolytes (CSEs) contribute to a more rigid membrane structure. Compared to PE, PEL not only enhances the solid–solid contact between the electrodes and the electrolyte but also reduces the risk of lithium dendrites penetrating the electrolyte, thereby broadening the potential applications of lithium batteries.

The prepared PVDF-HFP-based composite solid polymer electrolyte morphology was characterized using scanning electron microscopy (SEM). Figure 3a,c,e,g show the surface and cross-sectional SEM images of the PE membrane. The PE surface exhibits polymer agglomeration without pore structures, resulting in a relatively smooth surface, essential for maintaining good contact between the membrane and the electrodes. After further adding LLZTO to the electrolyte membrane, the electrolyte surface developed abundant pores. These pores facilitate the accommodation of the necessary electrolyte and provide more lithium-ion (Li^+) pathways, thereby enhancing lithium ion transport efficiency (Figure 3b,d,f,h).

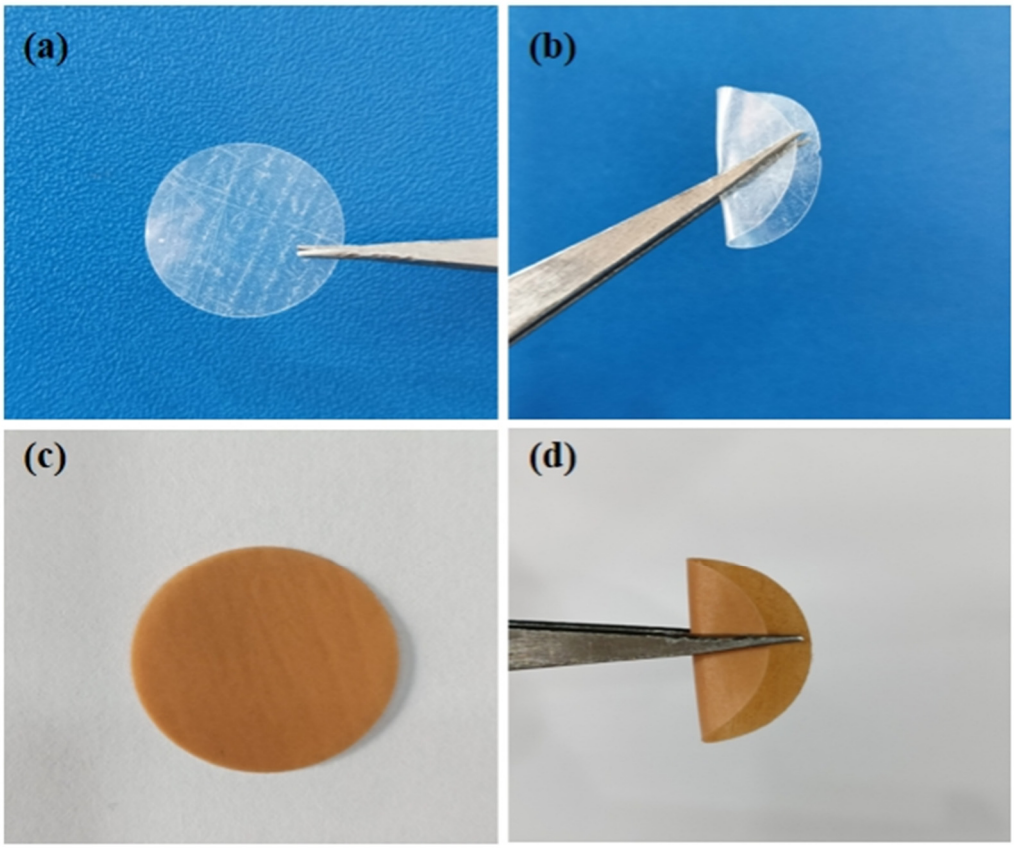

Figure 2. Images of (**a**,**b**) PE and (**c**,**d**) PEL solid electrolyte membranes.

The XRD patterns of LLZTO, PVDF-HFP, ETPTA, and PEL are shown in Figure 4a. The X-ray diffraction (XRD) patterns reflect the crystalline structure of the samples. In the XRD pattern of PVDF-HFP, diffraction peaks at 2θ = 18.8°, 20.5°, 27.1°, and 39.2° correspond to the (100), (020), (021), and (200) crystal planes, indicating its semicrystalline nature. The PEL pattern exhibits diffraction peaks characteristic of the cubic phase LLZTO. The peaks for LLZTO powder match those of the cubic garnet $Li_5La_3Nb_2O_{12}$ (PDF#45-0109), confirming LLZTO as a typical cubic phase. Comparing the PEL composite solid electrolyte with LLZTO, PVDF-HFP, and ETPTA reveals that blending these materials reduces crystallinity, thus increasing the amorphous regions, which is beneficial for enhancing lithium-ion transport and improving ionic conductivity. In Figure 4b, the PVDF-HFP-ETPTA (PE) membrane shows only a broad peak around 20°, indicating relatively low crystallinity. The introduction of the ETPTA cross-linking network likely reduces the crystallinity of the PVDF-HFP chains. Various amounts of LLZTO were added to PE, specifically 0 wt.%, 5 wt.%, 10 wt.%, 15 wt.%, and 20 wt.%. As the LLZTO content increased, the peak intensity first decreased and then increased, demonstrating that LLZTO addition effectively lowers the crystallinity of the PE electrolyte. The results indicate that when the LLZTO content is 10 wt.%, the PEL composite solid electrolyte exhibits the minimum peak intensity and lowest crystallinity, expanding the amorphous region and enhancing lithium-ion transport capacity. This provides strong evidence that adding LLZTO improves ionic conductivity, lithium-ion transference number, and other electrochemical properties.

Figure 4c presents the infrared absorption spectra of the PE polymer solid electrolyte. Before UV irradiation, two FTIR peaks at 1618 cm^{-1} and 1638 cm^{-1} are observed, attributed to the acrylate C=C bonds of the ETPTA monomer. After UV exposure, these peaks disappear, with no new peaks forming, confirming the successful polymerization of the ETPTA monomer in the precursor mixture. The infrared spectra of the prepared PEL were analyzed to investigate the impact of the active filler LLZTO on PE. Figure 4d displays the FTIR spectra of both PE and PEL. The results indicate that the α-phase crystal of PVDF-HFP cor-

responds to peaks in the 761 cm^{-1} to 983 cm^{-1} range, with an absorption peak at 835 cm^{-1} attributed to the β-phase vibrations and a characteristic peak at 877 cm^{-1} arising from vibrations of the β and γ phases. The peak at 1170 cm^{-1} represents the -CF_2 vibrations, while the peak at 1402 cm^{-1} corresponds to -CH_2 bending vibrations. A strong absorption peak at 1725 cm^{-1} for ETPTA indicates the carbonyl (C=O) stretching vibrations, which are known to facilitate Li^+ migration. To confirm the effect of LLZTO incorporation on the structure of the PVDF-HFP polymer substrate, the FTIR characterization of PEL shows that the intensities of these characteristic peaks in PE decrease with the addition of LLZTO nanoparticles, indicating a reduction in crystallinity of PVDF-HFP. However, the PEL membrane displays similar peaks to the PE membrane, suggesting that LLZTO nanoparticles and other components form a simple physical mixture with reactive interactions among the functional groups.

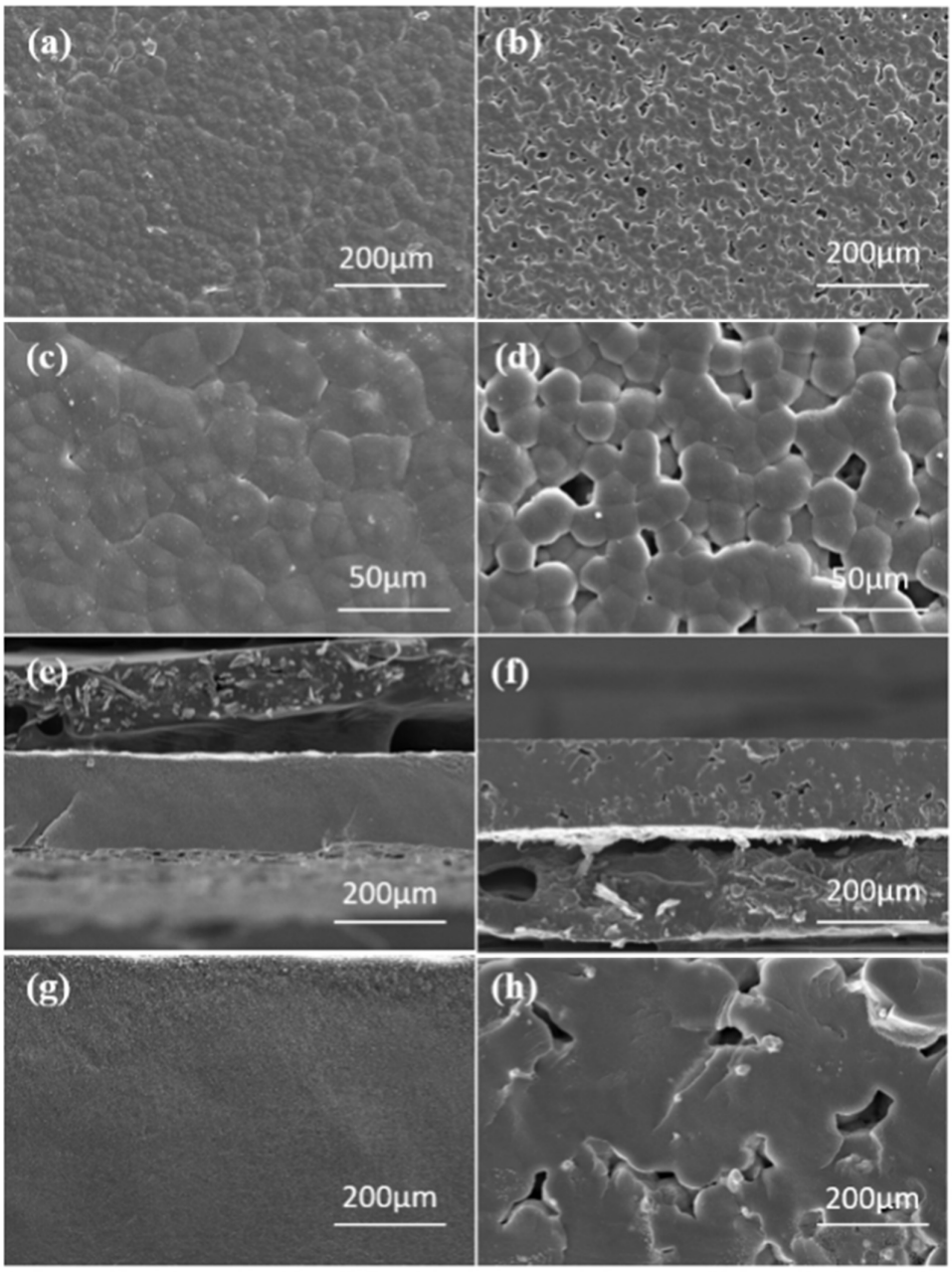

Figure 3. Surface topography of (**a**,**c**) PE; (**b**,**d**) surface topography of PEL; (**e**,**g**) cross-sectional morphology of PE; and (**f**,**h**) cross-sectional morphology of PEL.

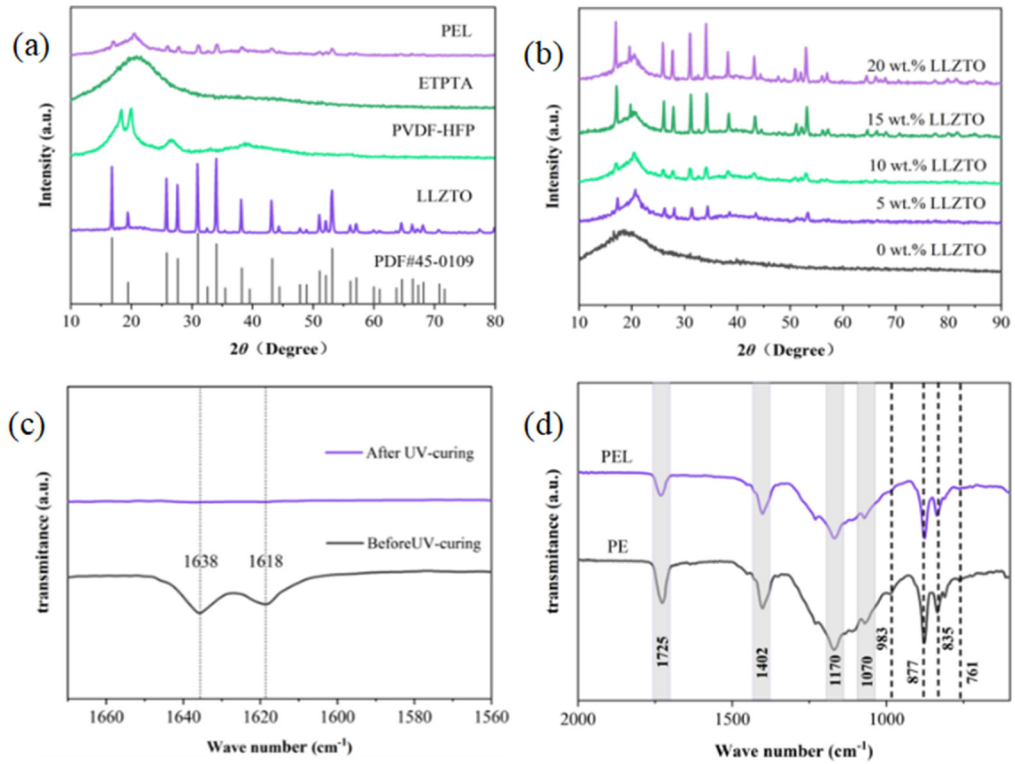

Figure 4. (**a**) X−ray diffraction spectra of LLZTO, PVDF−HFP, ETPTA, and PEL; (**b**) X−ray diffraction spectra of adding 0−20 wt.% LLZTO; FTIR infrared spectrum characterization diagram; (**c**) PE and PEL before and after UV photofixation; and (**d**) PE and PEL.

During the battery charge–discharge cycles, the continuous deposition and removal of lithium ions can lead to uneven deposition, resulting in moss-like or dendritic lithium growth at the interface between the electrode and the solid electrolyte. This unevenness increases internal stress within the battery and may also subject the electrolyte to excessive localized pressure, potentially leading to penetration by lithium dendrites. These adverse reactions significantly impede the battery's regular operation and pose a significant threat to its stability. To address these issues, the prepared solid electrolytes underwent stress-strain testing to investigate their elongation at break and tensile strength. As shown in Figure 5a, the tensile strength of the PE electrolyte membrane is 10.9 MPa, with a break elongation of 319%, demonstrating good flexibility. The PEL electrolyte membrane exhibits a tensile strength of 17.7 MPa and a break elongation of 198%. Although PEL's break elongation is lower than PE's after adding LLZTO, its tensile strength has nearly doubled. This improvement is attributed to the strong interactions between the inorganic nanoparticles and the polymer matrix, which restrict the movement of polymer chain segments and increase steric hindrance between molecular chains [32]. The enhanced tensile strength of PEL can enhance segment movement and facilitate ion conduction [33]. Moreover, the improved tensile strength of PEL is beneficial in suppressing lithium dendrite growth [34], thereby improving the cycling stability of lithium-ion batteries. Overall, the PEL composite membrane demonstrates good mechanical strength, adequately meeting the mechanical performance requirements for solid electrolyte materials in lithium-ion batteries.

Ionic conductivity is crucial for evaluating lithium-ion mobility in composite solid electrolyte membranes. Electrochemical impedance spectroscopy (EIS) was conducted to assess the ionic conductivities of four electrolyte membranes. The trivalent vinyl groups in ETPTA provide a new platform for UV curing due to their excellent curing activity and efficiency, allowing for the construction of interpenetrating networks that serve as a mechanical framework. In this process, the macromolecular monomer ETPTA was incorporated into PVDF-HFP, initiating polymerization under UV light to form a network

structure, resulting in a semi-interpenetrating polymer electrolyte. As shown in Figure 5b, the EIS impedance spectra revealed bulk resistances of 643 Ω, 525 Ω, 342 Ω, and 354 Ω for the different formulations. Notably, the minimum bulk resistance was observed when the PVDF-HFP to ETPTA ratio was 2:1. As the ETPTA content continued to increase, the bulk resistance showed an upward trend. This observed effect can be attributed to the excess macromolecular monomer ETPTA, which leads to internal molecular aggregation and a subsequent increase in resistance.

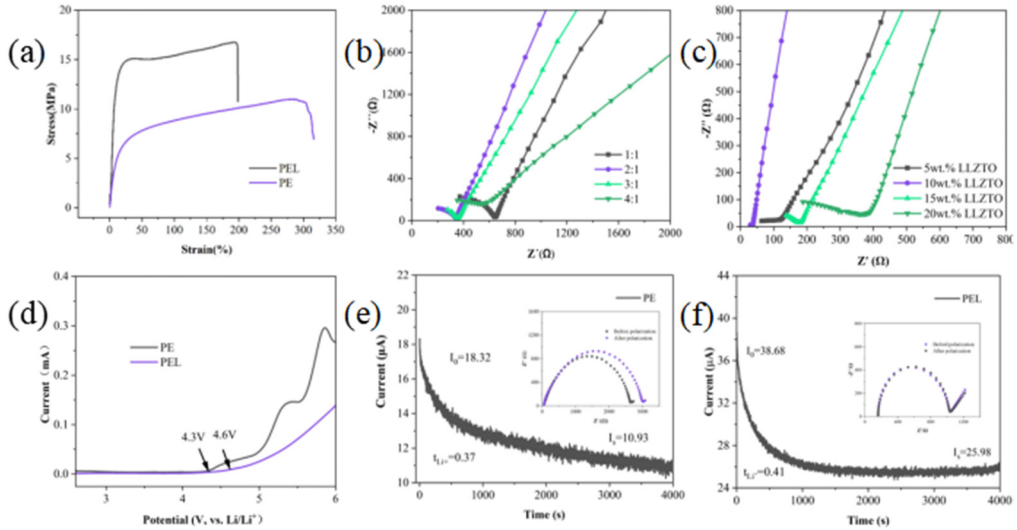

Figure 5. (**a**) Stress–strain plot of PE and PEL; EIS at room temperature; (**b**) PE electrolyte with different amounts of ETPTA added; (**c**) PEL electrolyte with different amounts of LLZTO added; (**d**) the linear sweep voltammetry of PE and PEL. Electrochemical impedance spectroscopy (EIS) and timing current method (CA) test the lithium-ion migration number of the assembled Li/Li symmetrical cells (**e**) PE and (**f**) PEL.

The high ionic conductivity of the oxide LLZTO, when blended with the polymer PVDF-HFP, enhances the electrochemical performance of the composite solid electrolyte. Four solid electrolyte membranes were prepared by adding varying amounts of LLZTO (5 wt.%, 10 wt.%, 15 wt., and 20 wt.%). Figure 5c shows that the bulk resistance of the four different electrolytes initially decreases and then increases with the addition of LLZTO—the electrolyte membrane with 10 wt.% LLZTO exhibits the minimum bulk resistance of 36 Ω. According to Table 1, the ionic conductivities calculated using formula (1) increase from 1.3×10^{-4} S cm^{-1} to 5.1×10^{-4} S cm^{-1}, then decrease to 6.3×10^{-5} S cm^{-1} and 2.6×10^{-5} S cm^{-1} as the LLZTO content increases. Table 2 shows a comparison of PAP/PEP membranes with existing solid-state electrolytes. These results indicate that incorporating LLZTO particles improves the ionic conductivity of the electrolyte membrane. This enhancement is attributed to the added LLZTO facilitating Li^+ transport pathways, allowing more Li^+ ions to move freely within the electrolyte, thus increasing its ionic conductivity. Research shows that the ionic conductivity of polymer electrolytes primarily depends on the crystallinity of the polymer chain structure. Uniformly dispersed LLZTO ceramic particles can hinder the reconfiguration of polymer chains, suppress crystallization, and create amorphous regions that accelerate ion transport. However, as the LLZTO content continues to increase, the ionic conductivity decreases due to excessive aggregation of LLZTO particles, which prevents their uniform distribution within the polymer matrix and obstructs the rapid transport of Li^+ ions within the electrolyte membrane.

The electrochemical stability of an electrolyte membrane is primarily indicated by its electrochemical stability window. Under normal battery operating conditions, this window is defined as the voltage range over which the current remains stable. When the voltage exceeds this window, resulting in a sharp increase in current, it indicates that the electrolyte

is undergoing oxidative decomposition, marking the limits of voltage that the membrane can tolerate and signaling the beginning of battery failure. As shown in Figure 5d, the linear sweep voltammetry curves illustrate the electrochemical stability windows for PE and PEL membranes. The current for the PE composite solid electrolyte membrane begins to rise rapidly after 4.3 V. In contrast, the introduction of LLZTO increases the electrochemical stability window of the PEL composite solid electrolyte membrane from 4.3 V to 4.6 V. This improvement demonstrates that the PEL composite polymer electrolyte membrane has a wider electrochemical stability window compared to the PE polymer solid electrolyte membrane. LLZTO particles effectively adsorb trace amounts of residual moisture in the electrolyte, thereby preventing decomposition at high voltages. Generally, the standard operating voltage for lithium-ion batteries is around 4.0 V, making the electrochemical stability windows 4.3 V for the PE membrane and 4.6 V for the PEL membrane compliant with the operational standards for lithium-ion batteries.

Table 1. The ion conductivity calculation data.

LLZTO Content (wt. %)	Bulk Impedance (Ω)	Ionic Conductivity (S/cm)
5%	93	1.3×10^{-4}
10%	36	5.1×10^{-4}
15%	177	6.3×10^{-5}
20%	359	2.6×10^{-5}

Table 2. Comparison with existing solid-state electrolytes.

SSEs	Ionic Conductivity ($\times 10^{-4}$ S/cm)	Ref.
PLP	2.57 (30 °C)	[35]
PPPL-10	4 (25 °C)	[36]
SSCEs	2.91 (25 °C)	[37]
PCEs-40-10-40	4.61 (60 °C)	[38]
PAN-10%LLZTO-PE	2.28 (25 °C)	[39]
PEL	4.27 (RT)	This work

The lithium-ion transference number is the ratio of lithium ions to the total number of ions within a specified time frame, and it plays a crucial role in the performance and operation of lithium batteries. A high lithium-ion transference number in the electrolyte effectively reduces concentration polarization, promotes uniform lithium-ion flow, and optimizes the environment for the extraction and insertion processes, thereby enhancing the cycling stability of the battery. Electrochemical impedance spectroscopy (EIS) and chronoamperometry (CA) were used to test the assembled Li/PE/Li and Li/PEL/Li batteries, resulting in Figure 5e,f. The lithium-ion transference number for the polymer solid electrolyte PE is 0.37, while for the composite solid electrolyte PEL, it is 0.41, significantly higher than the ~0.2 reported for conventional liquid electrolytes [40]. The notable increase in PEL's lithium-ion transference number can be attributed to two main factors. First, the cross-linked network formed by the addition of ETPTA restricts the movement of anions. Second, the uniform dispersion of the garnet-type filler LLZTO within the polymer matrix effectively reduces the crystallinity of the matrix and increases the proportion of the amorphous region in PVDF-HFP. This structural change optimizes the transport efficiency of lithium ions within the composite electrolyte. Furthermore, LLZTO, as an inorganic solid electrolyte, possesses a high transference number ($t_{Li}{}^{+} \approx 1$). Its introduction as an additive provides additional conduction pathways for lithium ions, further enhancing the ionic conductivity of the entire system.

To evaluate the impact of the inorganic filler LLZTO on the rate performance of solid-state electrolytes, standard CR 2025-coin cells were assembled using two types of electrolytes: PE and PEL. We conducted electrochemical tests at room temperature, measuring

discharge rates ranging from 0.1 to 1 C. As shown in Figure 6a, PEL demonstrated superior capacity compared to PE at discharge rates of 0.1 C, 0.2 C, 0.5 C, and 1 C. After high-rate cycling at 1 C, the PEL battery retained a capacity of approximately 20 mAh g^{-1}, while the PE battery failed to function, dropping to 0 mAh g^{-1}. This indicates that the modified solid electrolyte offers more favorable ionic pathways for high current discharge. Figure 6b presents the initial charge–discharge curves of the LFP/PEL/Li solid-state battery within a voltage range of 2.8 to 4.0 V at different rates. The curves are stable across varying rates, demonstrating good rate performance. Figure 6c compares the cycling performance of the batteries at a current density of 0.1 C. The initial discharge capacity of the LFP/PE/Li solid-state battery was 119 mAh g^{-1}, which decreased to 86 mAh g^{-1} after 100 cycles, resulting in a capacity retention rate of 72%.

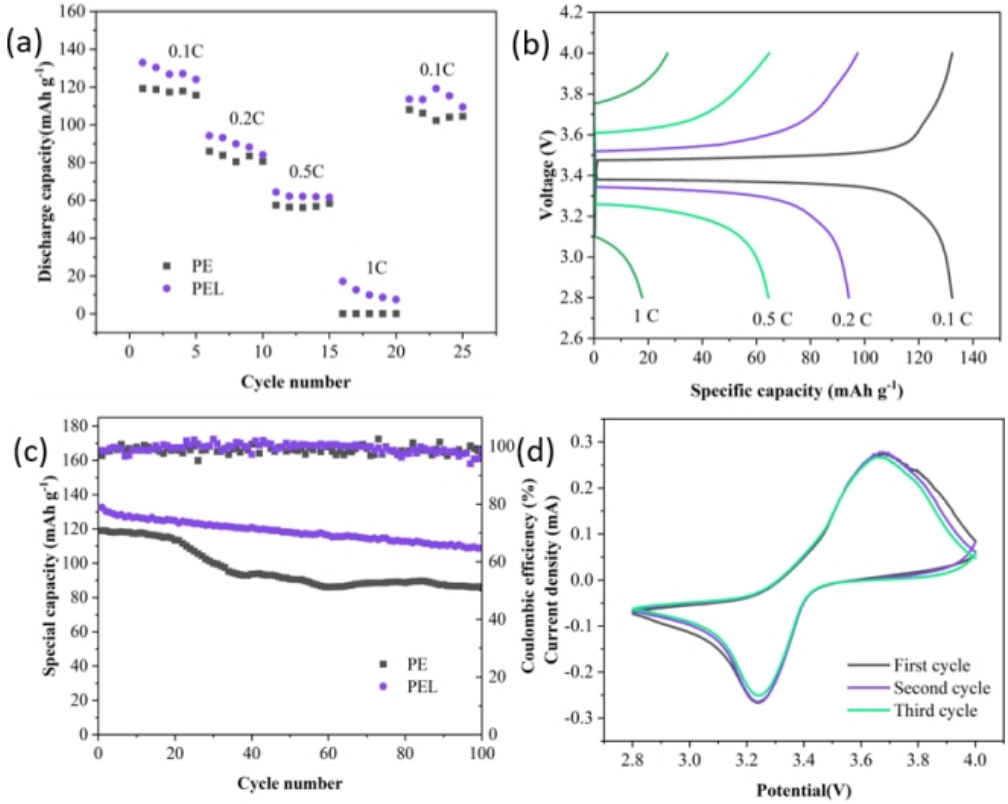

Figure 6. (**a**) Rate performance of LFP/PEL−PMEL/Li and LFP/PEL−PMEL/Li solid−state batteries at different rates; (**b**) first charge/discharge curves at different ratios of LFP/PEL−PMEL/Li; (**c**) cycling performance of the LFP/PEL−PMEL/Li and LFP/PEL−PMEL/Li solid−state batteries and (**d**) cyclic voltammetry curves of LFP/PEL−PMEL/Li solid−state batteries.

In contrast, the LFP/PEL/Li solid-state battery, after incorporating the inorganic filler LLZTO, showed an initial discharge capacity of 132 mAh g^{-1} at 0.1 C and maintained a capacity of 108 mAh g^{-1} after 100 cycles, achieving a capacity retention rate of 81%. This indicates that the PEL composite solid electrolyte exhibits better cycling stability and reversible capacity than the PE polymer electrolyte. Additionally, as depicted in Figure 6d, the cyclic voltammetry (CV) results reveal oxidation and reduction peaks at 3.68 V and 3.24 V, respectively, corresponding to the intercalation and de-intercalation of lithium ions in the LFP cathode material. Notably, the enhanced intensity of these peaks during three LFP/PEL/Li battery scans suggests that incorporating LLZTO facilitates faster lithium-ion diffusion.

4. Conclusions

We successfully synthesized a composite solid electrolyte using UV curing technology in this study. This electrolyte features a semi-interpenetrating network structure composed of a cross-linked ETPTA network, linear PVDF-HFP, and inorganic filler LLZTO. Electrochemical impedance spectroscopy revealed that the optimal ratio of PVDF-HFP to ETPTA is 2:1. Based on the PE formulation, we found that when LLZTO content is at 10 wt.%, the composite solid electrolytes exhibit the highest ionic conductivity of 5.1×10^{-4} S cm^{-1}, a wide electrochemical window of 4.6 V, and a lithium-ion transference number of 0.41. Additionally, the PEL electrolyte demonstrates a high tensile strength of 17.7 MPa. The LFP/PEL/Li solid-state battery showcases excellent capacity, rate capability, and cycling performance, with an initial discharge capacity of 132 mAh g^{-1} at 0.1 C. After 100 charge–discharge cycles, the capacity remains at 108 mAh g^{-1}, yielding a retention rate of 81%. Therefore, solid electrolytes designed with this approach hold promise for enhanced electrochemical performance, contributing to the practical development of safe, high-energy lithium-ion batteries.

Author Contributions: Conceptualization, M.H. and L.L.; methodology, P.S.; software, Z.L.; validation, M.H., P.S. and F.W.; formal analysis, L.L. and Z.L.; investigation, P.S., F.W. and Y.Z.; resources, Y.Z.; data curation, P.S.; writing—original draft preparation, P.S.; writing—review and editing, P.S. and Q.H.; visualization, Y.Z. and F.K.; supervision, C.W. and Q.H.; project administration, F.K.; funding acquisition, M.H., L.L., and C.W. All authors have read and agreed to the published version of the manuscript.

Funding: This research was funded by the Project of Basic and Applied Basic Research Projects of Guangzhou Basic Research Plan in 2023 (No. 2023A04J0677), the Fund Project of the Guangxi Key R&D Programme Projects (No. AB24010346), Reginal Collaboration R&D Program of Sichuan Province under Grant (No. 2024YFHZ0209), National Natural Science Foundation of China (No. 52161033, 22462003, 22262005), the Guangxi key laboratory of Automobile Components and Vehicle Technology (2023GKLACVTZZ02), and Major research projects of Liuzhou Polytechnic University (No. 2024KA01).

Data Availability Statement: The original contributions presented in this study are included in the article. Further inquiries can be directed to the corresponding authors.

Acknowledgments: This research was supported by the Project of Basic and Applied Basic Research Projects of Guangzhou Basic Research Plan in 2023 (No. 2023A04J0677), the Fund Project of the Guangxi Key R&D Programme Projects (No. AB24010346), Reginal Collaboration R&D Program of Sichuan Province under Grant (No. 2024YFHZ0209), National Natural Science Foundation of China (No. 52161033, 22462003, 22262005), the Guangxi key laboratory of Automobile Components and Vehicle Technology (2023GKLACVTZZ02), and Major research projects of Liuzhou Polytechnic University (No. 2024KA01).

Conflicts of Interest: The authors declare no conflicts of interest.

References

1. Alamdar, S.; Zarif, M. Exploring lithium salt solution in sulfone and ethyl acetate-based electrolytes for Li-ion battery applications: A molecular dynamics simulation study†. *J. Mater. Chem. A* **2024**, *12*, 17471–17482. [CrossRef]
2. Liu, Y.; Pan, Y.J.; Wang, H.C.; Li, H.G.; Bao, H.H.; Zhao, Z.W.; Liu, B.H. Mechanical issues of lithium-ion batteries in road traffic conditions: A review. *Thin-Walled Struct.* **2024**, *201*, 111985. [CrossRef]
3. Wu, X.X.; Ma, J.; Wang, J.X.; Zhang, X.; Zhou, G.M.; Liang, Z. Progress, Key Issues, and Future Prospects for Li-Ion Battery Recycling. *Glob. Chall.* **2022**, *6*, 2200067. [CrossRef]
4. Xiao, X.; Wang, L.; Wu, Y.Q.; Song, Y.Z.; Chen, Z.H.; He, X.M. Cathode regeneration and upcycling of spent LIBs: Toward sustainability. *Energy Environ. Sci.* **2023**, *16*, 2856–2868. [CrossRef]
5. Mohan, I.; Raj, A.; Shubham, K.; Lata, D.B.; Mandal, S.; Kumar, S. Potential of potassium and sodium-ion batteries as the future of energy storage: Recent progress in anodic materials. *J. Energy Storage* **2022**, *55*, 105625. [CrossRef]
6. Liu, L.H.; Cheng, B.S.; Yang, Z.W.; Wang, H.F.; Yue, C.; Hu, F. Oxocarbon Organic Conjugated Compounds for Lithium-ion Batteries and Solar Cells: Progress and Perspectives. *Curr. Org. Chem.* **2020**, *24*, 200–215. [CrossRef]
7. Cao, W.J.; Qiu, Y.S.; Peng, P.; Jiang, F.M. A full-scale electrical-thermal-fluidic coupling model for li-ion battery energy storage systems. *Appl. Therm. Eng.* **2021**, *185*, 116360. [CrossRef]

8. Mu, T.; Wang, Z.Q.; Yao, N.; Zhang, M.; Bai, M.; Wang, Z.H.; Wang, X.; Cai, X.; Ma, Y. Technological penetration and carbon-neutral evaluation of rechargeable battery systems for large-scale energy storage. *J. Energy Storage* **2023**, *69*, 107917. [CrossRef]
9. Khan, F.; Rasul, M.; Sayem, A.; Mandal, N. Design and optimization of lithium-ion battery as an efficient energy storage device for electric vehicles: A comprehensive review. *J. Energy Storage* **2023**, *71*, 108033. [CrossRef]
10. Han, D.; Son, H.; Han, S.; Song, C.; Jung, J.; Lee, S.; Choi, S.; Song, W.; Park, S. Hierarchical 3D Electrode Design with High Mass Loading Enabling High-Energy-Density Flexible Lithium-Ion Batteries. *Small* **2023**, *19*, 2305416. [CrossRef]
11. Wang, H.C.; Duan, X.D.; Liu, B.H. The Anisotropic Homogenized Model for Pouch Type Lithium-Ion Battery Under Various Abuse Loadings. *ASME J. Electrochem. Energy Convers. Storage* **2021**, *18*, 021015. [CrossRef]
12. Cortada-Torbellino, M.; Elvira, D.G.; El Aroudi, A.; Valderrama-Blavi, H. Review of Lithium-Ion Battery Internal Changes Due to Mechanical Loading. *Batteries* **2024**, *10*, 258. [CrossRef]
13. Zhang, X.Y.; Sun, Q.W.; Zhen, C.; Niu, Y.H.; Han, Y.P.; Zeng, G.F.; Chen, D.J.; Feng, C.; Chen, N.; Lv, W.Q.; et al. Recent progress in flame-retardant separators for safe lithium-ion batteries. *Energy Storage Mater.* **2021**, *37*, 628–647. [CrossRef]
14. Zhang, J.J.; Yang, J.F.; Dong, T.T.; Zhang, M.; Chai, J.C.; Dong, S.M.; Wu, T.Y.; Zhou, X.H.; Cui, G.L. Aliphatic Polycarbonate-Based Solid-State Polymer Electrolytes for Advanced Lithium Batteries: Advances and Perspective. *Small* **2018**, *14*, 1800821. [CrossRef]
15. Song, C.; Li, Z.G.; Peng, J.; Wu, X.H.; Peng, H.; Zhou, S.Y.; Qiao, Y.; Sun, H.; Huang, L.; Sun, S.G. Enhancing Li ion transfer efficacy in PEO-based solid polymer electrolytes to promote cycling stability of Li-metal batteries†. *J. Mater. Chem. A* **2022**, *10*, 16087–16094. [CrossRef]
16. Zhao, M.K.; Zuo, X.X.; Ma, X.D.; Xiao, X.; Liu, J.S.; Nan, J.M. Self-supported PVdF/P(VC-VAc) blended polymer electrolytes for $LiNi_{0.5}Mn_{1.5}O_4$/Li batteries. *J. Membr. Sci.* **2017**, *532*, 30–37. [CrossRef]
17. Wang, J.; Yan, W.; Fu, J.J.; Wang, L.; Liu, B. Dynamic and Reversible Blending Interface on Polyoxovanadate Electrode for High-Performance Lithium-Ion Batteries. *ACS Appl. Mater. Interfaces* **2024**, *16*, 8098–8108. [CrossRef]
18. Balakrishnan, N.T.; Melepurakkal, A.; Das, A.; KT, M.K.; Subramaniam, M.; Shelke, M.; Pullanchiyodan, A.; Raghavan, P. Safety enhanced novel polymer electrolytes for lithium-ion battery: Anomalous output performance with long term cycling stability by doping and polymer blending. *Mater. Today Chem.* **2024**, *39*, 102121. [CrossRef]
19. Gong, X.; Xiao, Q.; Li, Q.Y.; Liang, W.C.; Chen, F.; Li, L.Y.; Ren, S.J. Cross-linked Electrospun Gel Polymer Electrolytes for Lithium-Ion Batteries. *Chin. J. Polym. Sci* **2024**, *42*, 1021–1028. [CrossRef]
20. Chen, Y.L.; Song, Z.L.; Liu, H.C.; Xu, H.; Xi, Y.C.; Yin, C.Q.; Li, X.M.; Ma, L.; Yan, P.X.; Zhou, L. Cross-Linking Synergistic Effects to Enhance the Comprehensive Properties of Electrospun Polyimide Nanofiber Membranes for Advanced Lithium-Ion Batteries. *ACS Sustain. Chem. Eng.* **2024**, *12*, 5953–5964. [CrossRef]
21. Li, M.Y.; Cheng, S.; Zhang, J.S.; Huang, C.; Gu, J.P.; Han, J.; Xu, X.; Chen, X.; Zhang, P.C.; You, Y. Poly(vinylidene fluoride)-based composite membranes with continuous metal–organic framework layer for high-performance separators of lithium-ion batteries. *Chem. Eng. J.* **2024**, *487*, 150709. [CrossRef]
22. Yang, Z.; Jiang, M.X.; Cui, C.; Wang, Y.X.; Qin, J.W.; Wang, J.; Wang, Y.X.J.; Mao, B.G.; Cao, M.H. In-situ cross-linking strategy for stabilizing the LEDC of the solid-electrolyte interphase in lithium-ion batteries. *Nano Energy* **2023**, *105*, 107993. [CrossRef]
23. Yang, L.; Zhang, H.; Xia, E.J.; Wu, Y.M.; Li, Z.C. PEO/Li_2ZrO_3 composite electrolyte for solid-state rechargeable lithium battery. *J. Energy Storage* **2023**, *65*, 107283. [CrossRef]
24. Ou, J.H.; Li, G.R.; Chen, Z.W. Improved Composite Solid Electrolyte through Ionic Liquid-Assisted Polymer Phase for Solid-State Lithium Ion Batteries. *J. Electrochem. Soc.* **2019**, *166*, A1785. [CrossRef]
25. Han, W.; Kim, T.; Yoo, B.; Park, H. Tunable Dielectric Properties of Poly(vinylidenefluoride-co-hexafluoropropylene) Films with Embedded Fluorinated Barium Strontium Titanate Nanoparticles. *Sci Rep.* **2018**, *8*, 4086. [CrossRef]
26. Basu, S.; Hwang, G.S. First-principles prediction of anomalously strong phase dependence of transport and mechanical properties of lithium fluoride. *Acta Mater.* **2022**, *235*, 118077. [CrossRef]
27. Ding, P.P.; Lin, Z.Y.; Guo, X.W.; Wu, L.Q.; Wang, Y.T.; Guo, H.X.; Li, L.L.; Yu, H.J. Polymer electrolytes and interfaces in solid-state lithium metal batteries. *Mater. Today* **2021**, *51*, 449–474. [CrossRef]
28. Xia, Q.; Yuan, S.G.; Zhang, Q.; Huang, C.; Liu, J.; Jin, H.Y. Designing the Interface Layer of Solid Electrolytes for All-Solid-State Lithium Batteries. *Adv. Sci.* **2024**, *11*, 2401453. [CrossRef]
29. Raju, M.M.; Altayran, F.; Johnson, M.; Wang, D.L.; Zhang, Q.F. Crystal Structure and Preparation of $Li_7La_3Zr_2O_{12}$ (LLZO) Solid-State Electrolyte and Doping Impacts on the Conductivity: An Overview. *Electrochem* **2021**, *2*, 390–414. [CrossRef]
30. Gu, Y.C.; Liu, H.Q. PVDF-HFP/LLZTO composite electrolytes with UV cure for solid-state lithium rechargeable batteries. *J. Solid State Electrochem.* **2023**, *27*, 2671–2679. [CrossRef]
31. Zhou, Z.H.; Sun, T.; Cui, J.; Shen, X.; Shi, C.; Cao, S.; Zhao, J.B. A homogenous solid polymer electrolyte prepared by facile spray drying method is used for room-temperature solid lithium metal batteries. *Nano Res.* **2023**, *16*, 5080–5086. [CrossRef]
32. Park, T.; Lee, S.; Kim, D.M. Low-Temperature Manufacture of Cubic-Phase $Li_7La_3Zr_2O_{12}$ Electrolyte for All-Solid-State Batteries by Bed Powder. *Crystals* **2024**, *14*, 271. [CrossRef]
33. Pei, F.; Huang, Y.M.; Wu, L.; Zhou, S.Y.; Kang, Q.; Lin, W.J.; Liao, Y.Q.; Zhang, Y.; Huang, K.; Shen, Y.; et al. Multisite Crosslinked Poly(ether-urethane)-Based Polymer Electrolytes for High-Voltage Solid-State Lithium Metal Batteries. *Adv. Mater.* **2024**, *2024*, 09269. [CrossRef] [PubMed]
34. You, D.L.; Lai, Z.W.; Wei, W.; Xiong, H.M. High-Voltage All-Solid-State Lithium Metal Batteries Enabled by Localized High-Salt-Concentration In-Chain Clustering Copolymer Electrolytes. *Adv. Funct. Mater.* **2024**, 2415464. [CrossRef]

35. Gao, L.X.; Tang, B.; Jiang, H.Y.; Xie, Z.J.; Wei, J.P.; Zhou, Z. Fiber-Reinforced Composite Polymer Electrolytes for Solid-State Lithium Batteries. *Adv. Sustain. Syst.* **2022**, *6*, 2100389. [CrossRef]
36. Wang, Y.; Chen, Z.; Wu, Y.X.; Li, Y.; Yue, Z.Y.; Chen, M.H. PVDF-HFP/PAN/PDA@LLZTO Composite Solid Electrolyte Enabling Reinforced Safety and Outstanding Low-Temperature Performance for Quasi-Solid-State Lithium Metal Batteries. *ACS Appl. Mater. Interfaces* **2023**, *15*, 21526–21536. [CrossRef]
37. Zou, K.; Cai, Z.; Ke, X.; Wang, K.L.; Tan, X.Q.; Luo, D.D.; Huang, F.; Wang, C.Y.; Cheng, J.K.; Xiao, R.G. Electrochemical properties of LATP ceramic electrolyte doped with $LiBiO_3$ sintering additive and its derived sandwich structure composite solid electrolyte. *Ionics* **2023**, *29*, 2665–2678. [CrossRef]
38. Guan, D.C.; Huang, Y.; He, M.M.; Hu, G.R.; Peng, Z.D.; Cao, Y.B.; Du, K. Multilayer PEO/LLZTO composite electrolyte enables high-performance solid-state Li-ion batteries. *Ionics* **2021**, *27*, 4127–4134. [CrossRef]
39. Xu, K.; Xu, C.; Jiang, Y.J.; Cai, J.H.; Ni, J.X.; Lai, C.Y. Sandwich structured PVDF-HFP-based composite solid electrolytes for solid-state lithium metal batteries. *Ionics* **2022**, *28*, 3243–3253. [CrossRef]
40. Zhou, P.; Zhang, X.K.; Xiang, Y.; Liu, K. Strategies to enhance Li+ transference number in liquid electrolytes for better lithium batteries. *Nano Res.* **2023**, *16*, 8055–8071. [CrossRef]